

Tailored charging protocol for densified lithium deposition and stable initially anode-free lithium metal pouch cells

Received: 23 February 2025

Accepted: 29 October 2025

Published online: 23 December 2025

 Check for updatesYuanming Liu^{1,2,3,5}, Xiaoguang Yin^{4,5}, Hexin Guo¹, Shuwei Wang¹,
Baohua Li¹✉ & Guohua Chen^{2,3}✉

The low mechanical strength and insufficient lithium-ion conductivity of solid-electrolyte interphase will incur inhomogeneous lithium deposition and eventually cause battery failure, hindering practical application of lithium metal batteries. Combining multiple characterization techniques and COM-SOL simulation, here we report that the commonly-adopted constant current charge protocol would result in formation of highly porous lithium metal negative electrode, leading to severe parasitic reactions. To ameliorate this problem, we propose a middle peak current charge protocol with a peak current in the middle of charging step, which could guide the nucleation and growth of densified lithium deposition with the derived solid-electrolyte interphase possessing significantly improved mechanical strength and Li⁺ ion conductivity. Therefore, coin-type initially anode-free lithium metal batteries could be stably cycled for 80 cycles (with 3 hours of charging and state-of-charge of ~70%). A 1.5 Ah initially anode-free Li metal pouch cell which delivers a specific energy of 400 Wh kg⁻¹ at 225 mA and with a capacity retention of 80% for 298 cycles (with 3 hours of charging and state-of-charge of 80%) is also demonstrated.

Lithium (Li)-ion batteries (LIBs) using graphite negative electrode have been widely used for portable electronic devices and automotive applications since their development in 1990s^{1,2}. However, the energy density of existing Li-ion batteries is far below the demands for ever-increasing markets, such as long-term transportation and grid-scale energy storage. Therefore, Li metal batteries (LMBs) with lithium metal negative electrode (LMNE, 3860 mAh g⁻¹) have been reconsidered for future applications³. However, for the high self-diffusion barriers of Li adatoms to form Li nuclei⁴ and the insufficient Li⁺ ion conductivities and mechanical strength of the solid electrolyte interphase (SEI) on LMNE⁵, the dendritic LMNE will be formed during the charge process of LMBs. The irregular surface curvature of LMNE will also boost the

formation of Li dendrites, and the high charge current will accelerate this process⁶. Extensive research on Li metal structure⁷, compatible electrolyte system^{8–11}, artificial SEI^{12,13} and current collectors^{14–18} has been carried out to improve the performance of LMBs. However, until today, the formation of porous Li metal, as well as the plating of dendritic Li, are still inevitable. In addition, it is still challenging to achieve large-scale processing of Li foil because of the sensitivity of lithium towards air humidity⁹. To this end, the initially anode-free LMBs (IAFLMBs), is highly desirable for the commercialization of LMBs. They are not only compatible with the existing battery infrastructure but also deliver the highest energy density among all the reported structural prototypes of LMBs^{20,21}. However, the volume

¹Guangdong Provincial Key Laboratory of Thermal Management Engineering & Materials, Tsinghua Shenzhen International Graduate School, Tsinghua University, Shenzhen, China. ²School of Energy and Environment, City University of Hong Kong, Kowloon, Hong Kong SAR, China. ³Department of Chemical and Biological Engineering, The Hong Kong University of Science and Technology, Clear Water Bay, Kowloon, Hong Kong SAR, China. ⁴School of Environmental Science and Engineering, Southern University of Science and Technology, Shenzhen, China. ⁵These authors contributed equally: Yuanming Liu, Xiaoguang Yin. ✉ e-mail: libh@sz.tsinghua.edu.cn; kechengh@ust.hk

expansion/contraction of LMNE during charge/discharge of IAFLMBs makes the surficial SEI of LMNE to break easily, particularly under industry-relevant conditions such as high cell capacity, fast charging rate and low stack pressure. This creates gaps in achieving high-performance IAFLMBs with high energy density²² even though a 0.23 Ah IAFLMBs with 80% of its capacity retention after 200 cycles was demonstrated²³. Therefore, despite tremendous efforts such as electrolyte engineering^{10,23–26} and test-pressure adjustment²¹, developing Ah-level IAFLMBs with stable cycle life and high specific energy remains challenging.

The cycling performance of traditional LIBs can be increased by using many advanced cycling protocols, especially under the fast-charging conditions^{27–29}. For LMBs, the charge/discharge current represents the plating/dissolution rate of LMNE, respectively. It has been reported that the small charging current is helpful in boosting the reversibility of LMNE^{30,31}, the small discharging current of LMBs can boost the void-free Li metal dissolution³², and their relative values will also influence the cycling performances of LMBs³³. A prominent study also showed that isolated Li can be reutilized by controlling the discharge protocols of LMBs^{34,35}. Besides, various charge protocols have been proposed to increase the cycling performance of lithium battery, for example, the pulsed current^{36,37}, the asymmetric bidirectional current³⁸, the two-step current³⁹, the self-heat current⁴⁰, the initially high current seeded Li metal growth^{41,42} and the simulated non-linear potentiodynamic battery charging protocols⁴³, and so on. Some of them have shown successes in industrial applications, while the underlying role of different charge protocols for LMBs remains poorly understood.

The electrochemical deposition of thin films on the substrates is generally in a “stressed” state, for example, Sn and Cu thin films^{44,45}. This has been shown as a universal phenomenon that exists in thin films deposition^{46–48}. The presence of compressive stress during Li plating process had also been identified, which would promote the growth of Li dendrite^{49,50}. Strategies have been developed to mitigate the stress of LMNE, including 1) utilization of stress-releasing substrate; 2) formation of mechanically strong SEI; and 3) small operating current density. The utilization of soft substrate⁴⁹ or hemisphere-like concaves⁵¹ is helpful in releasing the internal stress of LMNE. The small operating current density can not only decrease the stress load in LMNE⁴⁹, but also guide the formation of SEI with increased mechanical strength compared with that formed at large current density⁵² (Fig. 1a, b). Thus, the Li metal deposited at relatively small current densities holds a uniform and dense structure^{7,52,53}. However, the small charging current strongly limits the fast-charging capability of LMBs.

The internal stress of LMNE is proportional to the deposited capacity and current density, which is one of the main constraints to forming a densely packed structure. Meanwhile, the as-deposited Li atoms can also act as nucleation seeds and growth substrate for subsequent Li plating, guiding a more uniform deposition. Bearing such a correlation between internal stress and Li growth rate in mind, we propose a middle peak current (MPC) charge protocol for LMBs (Fig. 1c), with a peak current in the middle of the charging step to regulate Li deposition. With such an MPC protocol, the formed LMNE consists of a densified structure and with the derived SEI possessing high strength and Li ion conductivity, thus an Ah-level IAF Li metal pouch cell with industrial-level loading positive electrodes could retain 80% of its capacity even after 298 cycles.

Results

Methodology, cell performance, and morphology

The key to the MPC protocol is its small starting and ending currents, and peak current in the middle. Therefore, compared with the traditional constant current (CC) plating protocol (1 mA cm⁻², Fig. 1d, e), we designed an MPC protocol with its initial and final current densities being 0.5 mA cm⁻² and the middle current density being 2 mA cm⁻² in

Li||Cu cells (Fig. 1g, h). Note that the total plating time for both CC and MPC protocols is the same as 3 h. After the plating process, the deposited Li metal for both the CC and MPC protocols was stripped at 1 mA cm⁻². As shown in Fig. 1f, i, the MPC protocol delivers a much higher coulombic efficiencies (CEs) and data consistency than the CC protocol. In addition, the MPC protocol also demonstrates higher average CEs (Supplementary Fig. 1) and better cycling stability at 60 °C (Supplementary Fig. 2a), and higher CEs under an areal capacity of LMNE of 0.3 mAh cm⁻² (Supplementary Fig. 2b–d) or 6 mAh cm⁻² (Supplementary Fig. 2e–g). The comparison with many other existing charge protocols (Supplementary Figs. 3–4) further validates the effectiveness of the MPC charge protocol in stabilizing LMNE during repeated plating/stripping processes. Varying the position of the largest current density (Fig. 1d, e, g, h and Supplementary Fig. 5), the cell achieved the best performance when it was placed at the third step (Fig. 1f, i and Supplementary Fig. 6), demonstrating the effectiveness of MPC protocol.

The morphologies of deposited Li metal through CC and MPC plating protocols (Supplementary Table 1) in Li||Cu cells were characterized by scanning electron microscopy (SEM). When 0.25 mAh cm⁻² of Li metal was deposited at 0.5 mA cm⁻² (MPC1 sample, Fig. 2e, f), spherical Li metal morphology was observed, while the Li metal that was deposited at 1 mA cm⁻² was less spherical (CC1 sample, Fig. 2a, b). For the CC2 sample, the Li metal deposited through CC protocol exhibits a kind of porous structure (Supplementary Fig. 7). However, the Li metal deposited via MPC protocol always yields a densely packed structure (Supplementary Fig. 8). When the Li capacity increases to 3 mAh cm⁻² (theoretical thickness of ~12.9 μm), the Li metal deposited through CC protocol presents a porous “Zone 1” like structure (Fig. 2c) and delivers a thickness of 16.7 μm (Fig. 2d), which corresponds to a porosity of 22.9% and should be avoided for dense film growth⁵⁴. Conversely, for the Li metal film at the same capacity of 3 mAh cm⁻², the MPC protocol results in a denser “Zone 3” like structure (Fig. 2g) with a thickness of only 13.6 μm (Fig. 2h), which corresponds to a porosity of 5.4% only. As shown in Supplementary Fig. 9, the thickness of deposited Li through the MPC protocol is obviously smaller than the porous and loose Li metal structure formed by many other protocols (≥ 14 μm, with porosity ≥ 8.1%). The densified lithium could thus suppress the parasitic reactions with the electrolytes, leading to the formation of a thinner by-products layer (induced by the side-reactions between Li metal and electrolyte) than those by many other protocols after repeated cycling tests (Fig. 2j and Supplementary Fig. 9).

Apart from the deposition process of LMNE with relatively higher stack pressure in coin-type cells, Li deposition under smaller stack pressure is also important for practical application⁵¹. Therefore, a hollow PTFE spacer is added to characterize the Li metal morphologies at relatively ample space (Supplementary Fig. 10). Li grown through CC protocol shows a severe lumped structure regardless of the spacer thickness (200 or 300 μm). By contrast, Li metal formed through the MPC protocol tends to distribute uniformly. The lumped Li metal structure results from the centralized interaction between perpendicular dendrite growth and the pressure from the separator, which is undesirable for cell operation.

Mechanical strength, transport properties and compositions of SEI

Atomic force microscopy (AFM) was employed to characterize the microstructures and mechanical properties of the derived SEI by CC and MPC protocols. To minimize the random errors of modulus test that may be caused by the position variations of electrodes, we conducted the modulus tests at three positions of LMNE, as shown in Supplementary Fig. 11a. When we choose the test results at position 2 (i.e., the central area of the electrode) of different samples to make a comparison, the Young's modulus of the initial SEI (with Li capacity of

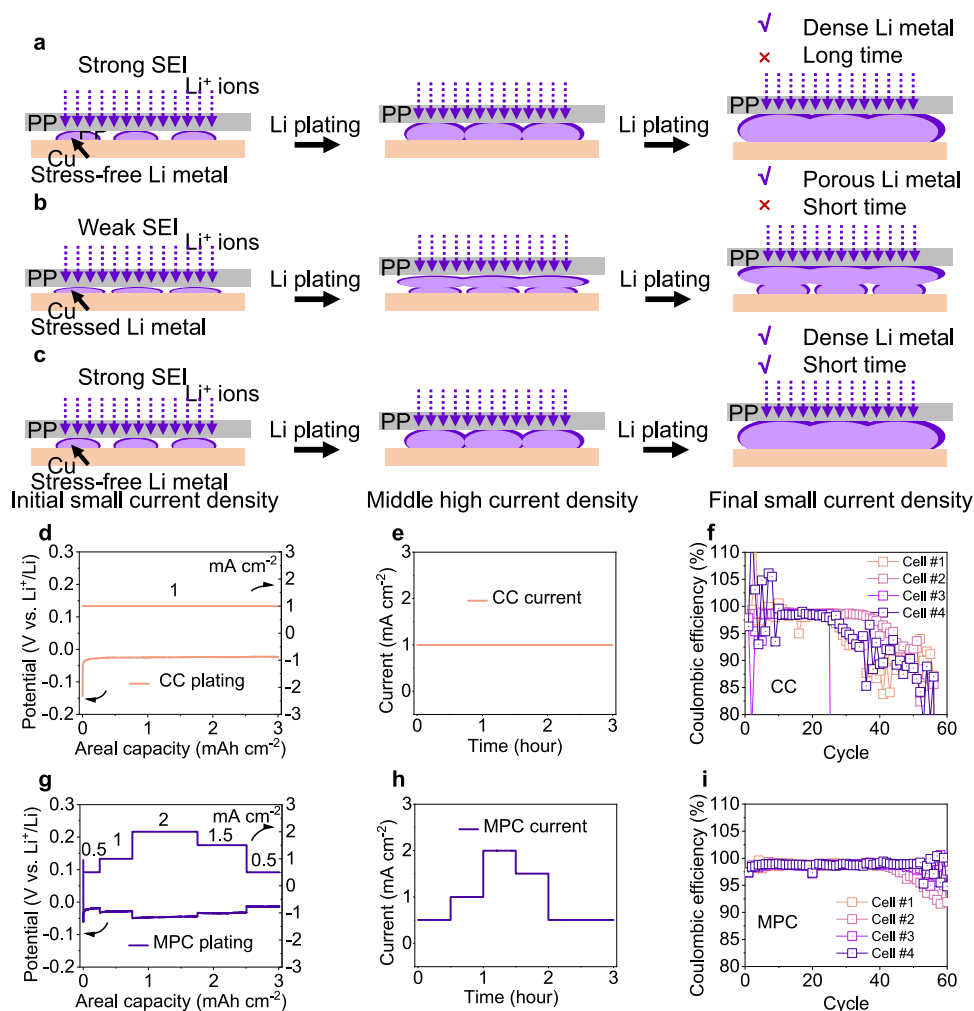


Fig. 1 | Methodology and performance. **a** Schematics showing the Li metal plating mechanism at a relatively small current. **b** Schematics showing the Li metal plating mechanism at a relatively large current. **c** Schematics showing the Li metal plating mechanism with middle peak current (MPC) pattern. **d, g** Potential-capacity and current density-capacity profiles for the constant current (CC) and MPC plating

protocols in Li||Cu cells, respectively. **e, h** Current density-time profiles for the CC and MPC plating protocols in Li||Cu cells, respectively. **f, i** Coulombic efficiencies (CEs) of Li||Cu cells where the Li metal was deposited through CC and MPC protocols, respectively. Four duplicates for each protocol were tested to minimize the operational errors.

0.25 mA h cm⁻² at 1 mA cm⁻² for CC1 (1.1 GPa, Fig. 2l) is lower than that formed at 0.5 mA cm⁻² for MPC1 (2.1 GPa, Fig. 2n). This shows that the SEI formed at smaller current density would possess a higher modulus. Moreover, when Li metal was deposited at 3 mA h cm⁻², the Young's modulus of the derived SEI via MPC protocol (MPC6 (5.3 GPa), Fig. 2o) is 89% higher than that formed by CC protocol (CC6 (2.8 GPa), Fig. 2m). Although the modulus of SEI will change with the positions where it is measured, the averaged values of MPC1 sample (2.3 GPa) and MPC6 sample (4.9 GPa) are respectively 130 and 96% higher than those of CC1 sample (1 GPa) and CC6 sample (2.5 GPa), demonstrating the advantage of MPC protocol in forming SEI with a high mechanical strength (Supplementary Fig. 11b and Supplementary Fig. 12). When the plated Li metal was fully stripped, the tested modulus of MPC1 sample is also higher than that of CC1 sample (Supplementary Fig. 13), aligns well with the above modulus analysis. The Young's modulus of the as-formed SEI on Li metal through MPC protocol is also much higher than that of SEI formed by other protocols (≤ 4 GPa, Fig. 2k and Supplementary Fig. 14). The PeakForce TUNA test of AFM characterizations was conducted to show the contact current of CC1, MPC1, CC6 and MPC6 samples, respectively, as shown in Supplementary Fig. 15. The results clearly show that the SEI formed on MPC1 sample has smaller electrical conductivity than that of CC1 sample, which means that the SEI formed at a small current density

(0.5 mA cm⁻², MPC1 sample) has better electrical insulation properties than the SEI formed at a large current density (1 mA cm⁻², CC1 sample). Even after 3 mA h cm⁻² of Li metal was deposited, the SEI on CC6 sample still delivers a higher electrical conductivity compared to that of the SEI formed on MPC6 sample. The above AFM characterization results clearly show that the MPC protocol can enable the formation of SEI with high modulus and low electrical conductivity, suppressing the formation of porous LMNE.

Apart from modulus, the lithium-ion diffusivity through the SEI also depends on the microstructures of deposited lithium. Temperature-varying electrochemical impedance spectrum (EIS) tests between -20 °C and 30 °C were carried out. The linear fitting between the natural logarithm of resistance and the reciprocal of temperature, namely Arrhenius relation ($\ln R = -\frac{E_a}{R} \frac{1}{T} + C$, C is a constant), can give the value of activation energy (E_a) for a specific process. Typically, the semi-circle of R_{SEI} in the high (10^5 Hz)-middle (10^3 Hz) range arises from the impedance of the interfacial film on Li metal, while the semi-circle of R_{De} in the low frequency range (10^3 Hz to 10^0 Hz) reflects the charge-transfer process (Supplementary Fig. 16a). Therefore, the activation energies $E_{a, SEI}$ and $E_{a, De}$, which were obtained by fitting the obtained R_{SEI} and R_{De} via Arrhenius relation, representing the transport process of Li⁺ ions in SEI film and the de-solvation process of Li⁺ ions, respectively⁵⁵. As shown in Supplementary Fig. 16b-m, for the SEI

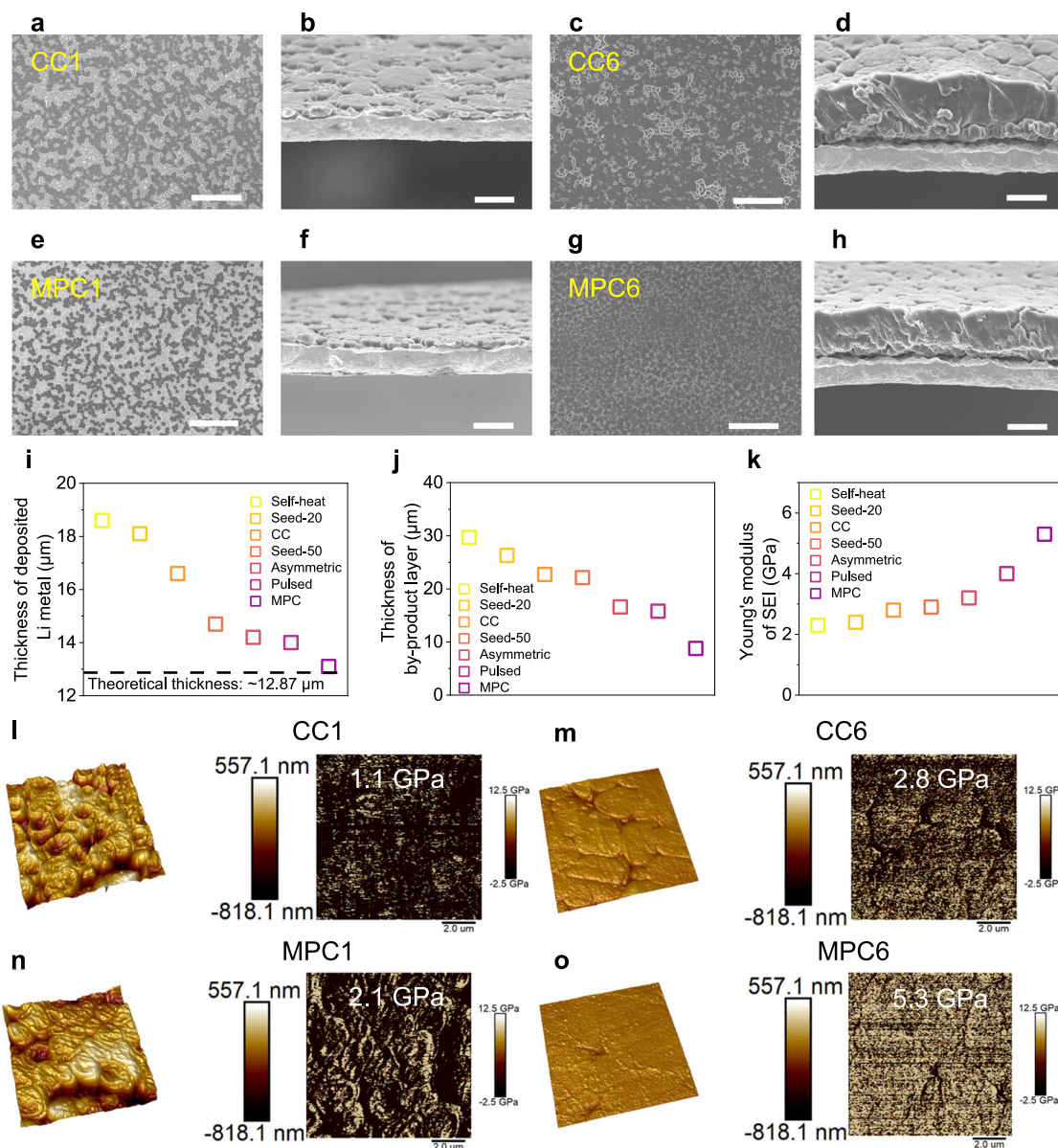


Fig. 2 | Plated Li morphologies and SEI properties in Li||Cu half cells. Front and Cross-sectional scanning electron microscope (SEM) images of **a, b** CC1 sample; **c, d** CC6 sample; **e, f** MPC1 sample and **g, h** MPC6 sample, respectively. Typically, these SEM images were captured at the 1st plating process after activating the Li||Cu half-cell five times at a current of 0.05 mA cm⁻² in between the potential of 0.01 V - 1 V vs. Li⁺/Li. **i, j, k**, Comparisons for the deposition thickness of Li metal (3 mAh cm⁻²), the thickness of the reaction by-product layer and the modulus for the SEI on the Li metal formed by various protocols in Li||Cu half cells, which include Self-heat-9 mA

cm⁻² (denoted as Self-heat), Seed current-20 mA cm⁻² (denoted as Seed-20), Constant current (denoted as CC), Seed current-50 mA cm⁻² (denoted as Seed-50), Asymmetric bidirectional current (denoted as Asymmetric), Pulsed current (denoted as Pulsed) and Middle peak current (denoted as MPC). Three-dimensional (3D) atomic force microscopic (AFM) images of the deposited Li metal and Young's modulus distribution maps (the inset is the mean value of each sample) of the as formed SEI on **l**, CC1; **m**, CC6; **n**, MPC1 and **o**, MPC6 samples, respectively. Scale bar length: **a, c, e, g**, 50 μm ; **b, d, f, h**, 10 μm .

formed on CC1 sample, the solvated Li⁺ ions would be de-solvated ($E_{a, De} = 38.6 \text{ kJ mol}^{-1}$) more easily compared to that of MPC1 sample ($E_{a, De} = 42.8 \text{ kJ mol}^{-1}$), while the transportation of Li⁺ ions through both SEIs are almost the same ($E_{a, SEI} = 65 \text{ kJ mol}^{-1}$ of CC1 sample compared to 65.8 kJ mol⁻¹ of MPC1 sample). However, for the SEI formed on the MPC6 sample, both the desolvation (36.4 kJ mol⁻¹) and transport of Li⁺ ions (59 kJ mol⁻¹) are easier than those of the CC6 sample (38.5 kJ mol⁻¹ for desolvation and 65.9 kJ mol⁻¹ for transport of Li⁺ ions, respectively). In addition, both the SEI diffusivity (D_S) and bulk diffusivity (D_B) of Li ions are important for Li metal morphology⁵⁶. Therefore, these two values are further examined (Supplementary note and Supplementary Table 2). It was found that the D_S/D_B values for both the CC1 and MPC1 samples are almost the same, while the final SEI formed via MPC

protocol delivers a much higher D_S/D_B value, which further ascertains the more favorable Li-ion transportations for the SEI formed by the MPC protocol.

X-ray photoelectron spectroscopy (XPS) depth-profiling analysis was further carried out to characterize the composition of SEI formed at different stages of CC and MPC protocols (Supplementary Figs. 17–23). As shown in Supplementary Fig. 17, there is an obvious increase in the carbon signal of CC3 sample compared with that of CC2 sample, and this may result from the increased side reactions between the formed porous Li metal (Supplementary Fig. 7) and electrolyte. As shown in Supplementary Fig. 18, although there is still an increase in carbon signal at the inner SEI of MPC3 sample compared to that of MPC2 sample and which may result from the high middle

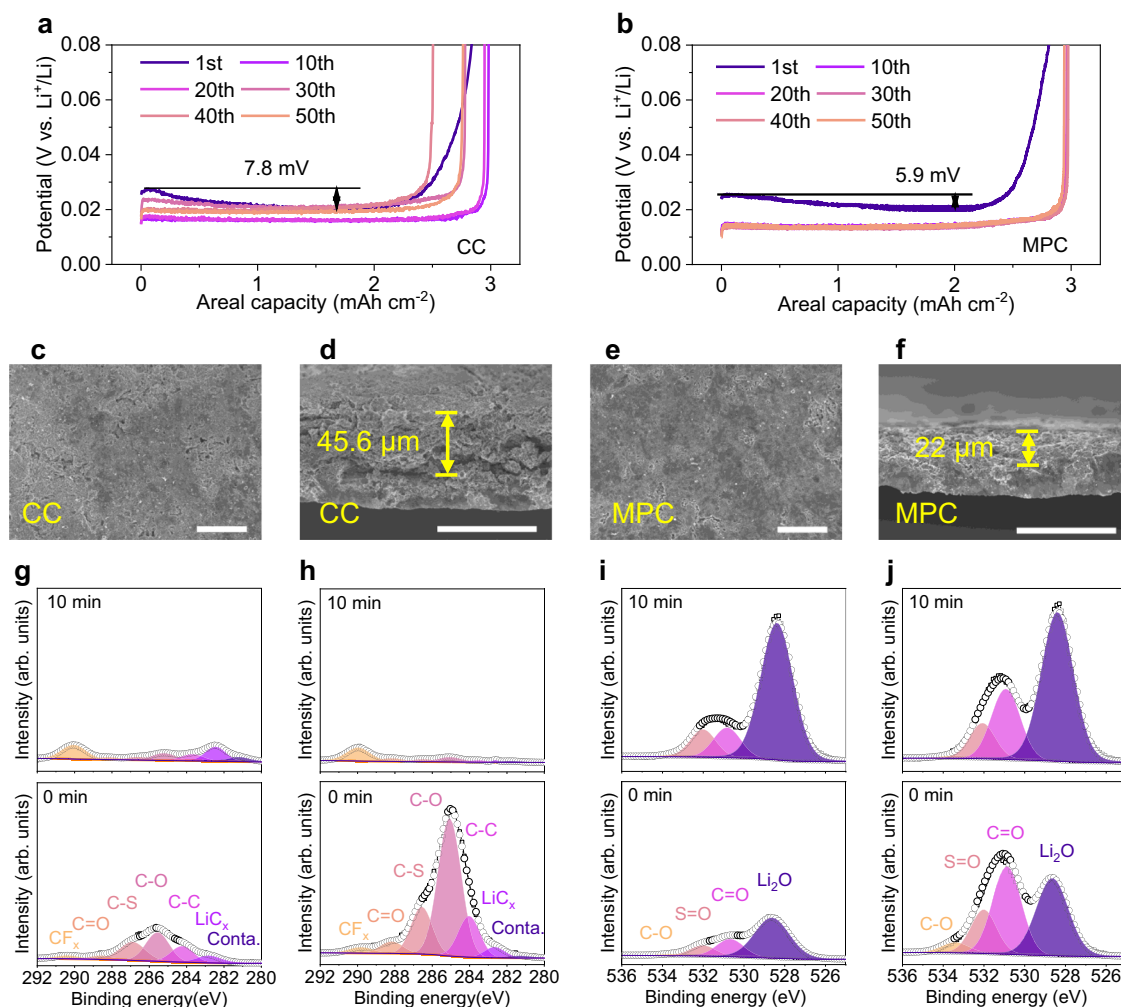


Fig. 3 | Morphologies and residual composition of cycled Cu in Li || Cu half cells.

a Potential-capacity profiles of the Li stripping process of Li || Cu cells through CC plating protocol. **b** Potential-capacity profiles of the Li stripping process of Li || Cu cells through MPC plating protocol. **c** Front and **d** Cross-sectional SEM images of the Cu foil in Li || Cu half-cell after being cycled 50 times through CC protocol (3 mAh cm⁻², 3 h). **e** Front and **f** Cross-sectional SEM images of the Cu foil in Li || Cu half-cell after being cycled 50 times through MPC protocol (3 mAh cm⁻², 3 h). **g** XPS depth profiles for the carbon (C) 1s spectra of the cycled Cu foil after 50 times through **g** CC and

h MPC protocols, respectively. XPS depth profiles for the oxygen (O) 1s spectra of the cycled Cu foil after 50 times through **i** CC and **j** MPC protocols, respectively. It is worth noting that for the CC protocol, cycled Cu foil in Li || Cu half-cell, the Li metal negative electrode was both plated and stripped via CC current, while for the MPC protocol, cycled Cu foil in Li || Cu half-cell, the Li metal negative electrode was plated via MPC current and stripped via CC current. The electrolyte used here is 1 M LiTFSI in DOL/DME (v/v, 1/1) with 1 wt% LiNO₃. Scale bar: **c, d, e, f**, 50 μm.

current accelerated solvent decomposition, the carbon signal for the SEI of MPC plated Li metal remains stable. For the O1s spectra, there are more contents of C=O in CC plated Li metal (Supplementary Fig. 19) compared to that of MPC plated Li metal (Supplementary Fig. 20). For the F1s XPS depth profiles, the SEI formed on CC1 sample is rich in surficial LiF content (Supplementary Fig. 21), differing from the inner LiF-rich while low LiF content structure of MPC1 sample (Supplementary Fig. 22). Apart from the modulus of SEI, the difference in LiF content between CC1 and MPC1 samples may also be the reason for the formation of porous Li metal structure of CC2 sample as shown in Supplementary Fig. 7b. The SEI formed by CC current has a high LiF content on its surface (Supplementary Fig. 21f), which is less favorable for Li-ion transportation because the Li-ion conductivity through LiF is very low. By contrast, the SEI formed under MPC current has low LiF content at its surface and high LiF content at its inner layer (Supplementary Fig. 22f), which is effective in blocking electron conduction without sacrificing Li ion transportation^{13,57}. It is worth noting that the final MPC-SEI is rich in inorganic Li compounds (mainly Li₂O, Supplementary Fig. 20f), which is different from the final CC-SEI with high organic C=O contents (Supplementary Fig. 19f). For the N1s XPS depth

profiles of CC-SEI and MPC-SEI, the MPC-SEI delivered a higher content (28.7%, Supplementary Fig. 23b) of highly conductive Li₃N compounds than CC-SEI (26.9%, Supplementary Fig. 23a), which may also contribute to the better Li-ion transport through MPC-SEI than that of CC-SEI. The post-mortem XPS analysis also showed that the Li₂O-rich SEI can be well retained at elevated temperature and after repeated cycling tests (Supplementary Figs. 24–27). The undesired Li stripping would produce dead Li, SEI crack, uneven interface, and so on. For the MPC plating protocol, the generated SEI has a high strength (modulus: 5.3 GPa) with an inorganic-rich structure dominated by Li₂O (inner- and outer-layer) and low LiF (while mainly inner layer). Therefore, the discharging of the MPC protocol deposited Li metal has lower stripping overpotentials (5.9 mV, Fig. 3b) compared with those from the CC samples (7.8 mV) (Fig. 3a). This is expected from the lithiophilic Li|Li₂O interface, which could attract the Li atoms quickly to fill the Li vacancies created by Li stripping near the Li|Li₂O interface and maintain a smooth Li surface^{32,58}.

The morphologies for the cycled Cu foils in Li || Cu half cells were also characterized by SEM and XPS. The cycled Cu foils in Li || Cu half cells through MPC protocol present more even surface

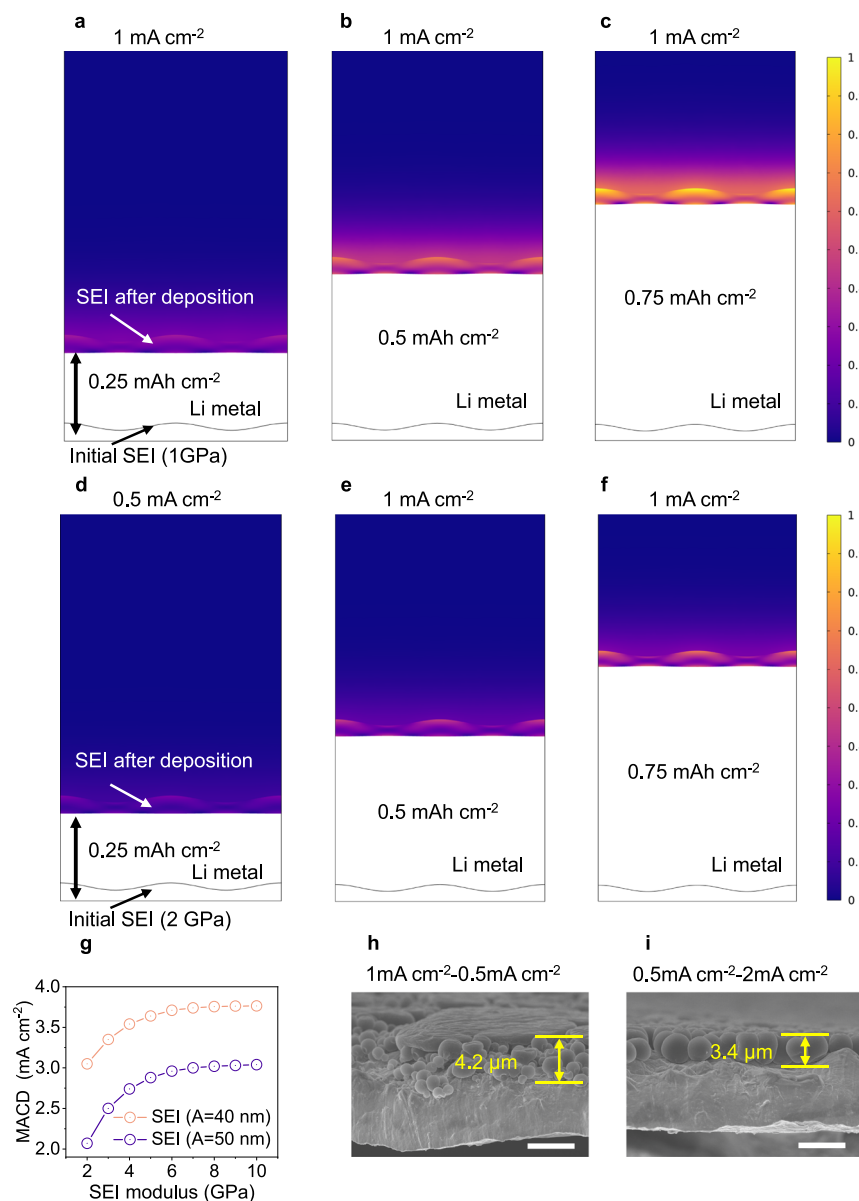


Fig. 4 | Simulation for the stress accumulation of SEI and Li metal morphologies. **a–c** Von Mises stress distribution of SEI ($y = 200 + A \cos \omega \pi x$, where $\omega = 1.3$ and $A = 40$ nm) after 0.25 mAh cm⁻², 0.5 mAh cm⁻² and 0.75 mAh cm⁻² of Li metal deposited at 1 mA cm⁻², respectively. **d–f** Von Mises stress distribution of SEI ($A = 40$ nm) after Li metal deposited at 0.5 mA cm⁻² (0.25 mAh cm⁻²), 0.5 mA cm⁻² (0.25 mAh cm⁻²)-1 mA cm⁻² (0.25 mAh cm⁻²) and 0.5 mA cm⁻² (0.25 mAh cm⁻²)-1 mA cm⁻² (0.5 mAh cm⁻²), respectively. **g** Maximum allowable current density (MACD) for 0.5 mAh cm⁻² of Li plating after 0.25 mAh cm⁻² of Li metal deposited at 0.5 mA cm⁻²

with different SEI modulus. SEM morphologies of Li metal (0.75 mAh cm⁻²) deposited at different schemes: **h** 1 mA cm⁻² (0.25 mAh cm⁻²)-0.5 mA cm⁻² (0.5 mAh cm⁻²); **i**, 0.5 mA cm⁻² (0.25 mAh cm⁻²) - 2 mA cm⁻² (0.5 mAh cm⁻²). These two SEM images were captured at the 1st plating process after activating the Li|Cu half-cell five times at a current of 0.05 mA cm⁻² in between the potential of 0.01 V-1 V vs. Li/Li. The normalized color scale next to panels Fig. 4c and Fig. 4f is based on the yield strength of each SEI. For example, for the SEI with modulus of 2 GPa, the 1 in the color scale represents the stress of 0.02 GPa. Scale bar: **h**, **i** 5 μm.

morphologies and thinner by-product layers (22 μm after 50 cycles and 2.1 μm after ten cycles) than those under CC protocol (45.6 μm after 50 cycles and 19.1 μm after ten cycles), respectively (Fig. 3c-f and Supplementary Fig. 28). For the composition of reaction by-products layer, the one after MPC protocol has low content of LiC_x, while the one using CC protocol is in clear contrast (Fig. 3g, h). The high contents of LiC_x may perforate through the separator, causing battery inefficiency and safety concerns⁵⁹. In addition, different from the CC charging protocol, the cycled Cu foil using the MPC protocol has higher surficial carbon content (mainly polymerized C-O and C=O groups, Fig. 3i, j), which is effective in protecting LMNE and re-activating the dead Li (see extended applications below).

COMSOL simulations for the maximum allowable current density

For practical usage, it is important to evaluate the largest plating current density that the as-formed SEI could sustain. To this end, COMSOL multiphysics simulation was carried out by combining the ternary current distribution, deformed geometry and solid mechanics modules (Fig. 4a-g, Supplementary Fig. 29 and Supplementary Table 3). It is worth noting that Fig. 4a-f are only part of the simulation cell (the observation window in Supplementary Fig. 29). Firstly, Li metal deposition process through CC and MPC protocols in Li|Cu half cells were simulated. Typically, the plating protocols of 1 mA cm⁻² (0.75 mAh cm⁻²) in comparison with 0.5 mA cm⁻² (0.25 mAh cm⁻²) - 1 mA cm⁻² (0.5 mAh cm⁻²) were simulated with the SEI modulus being 1

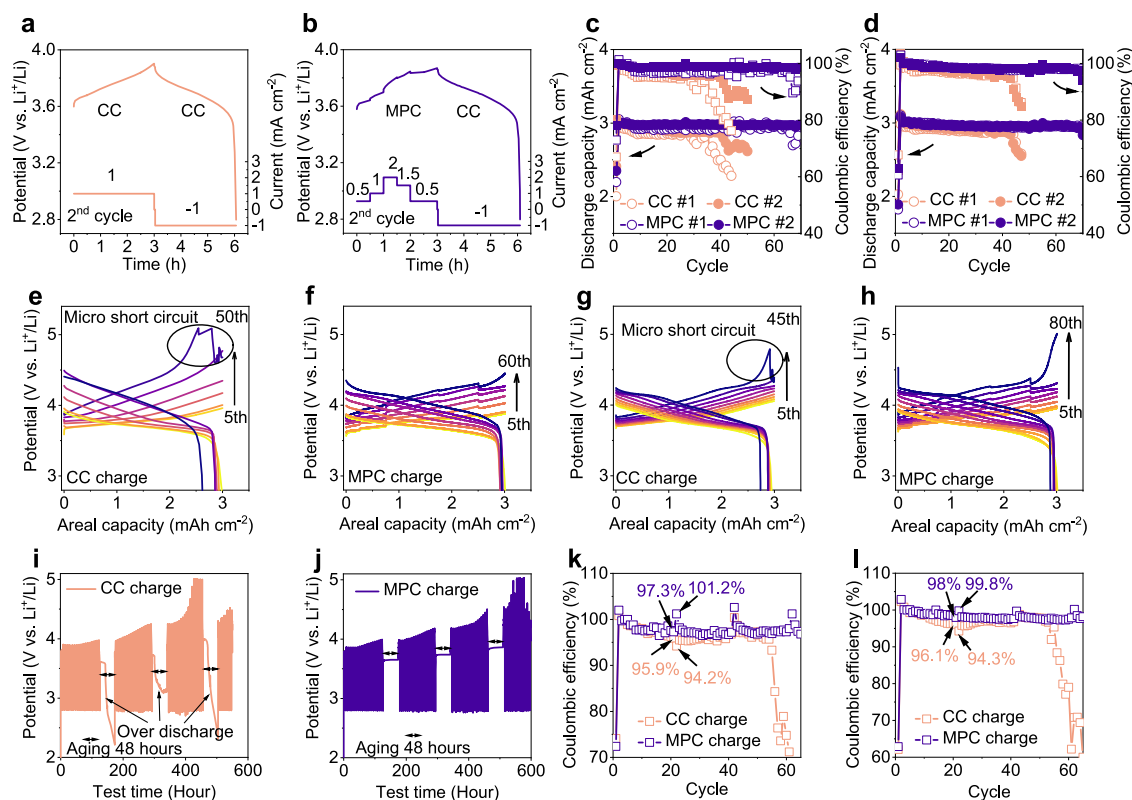


Fig. 5 | Cycling performance and extended applications. **a, b** Charge-discharge potential-time profiles of IAF Li metal coin cells coupled with high loading NMC622 positive electrodes at the second cycle charged through CC and MPC protocols, respectively. Discharge capacities and Coulombic efficiencies of IAF Li metal coin cells using different charging protocols with high loading **c** NMC622 positive electrodes and **d** SCNMC811 positive electrodes, respectively. **e, f** Potential-capacity profiles of IAF Li metal coin cells with high loading NMC622 positive electrodes and charged through CC (CC #1) and MPC (MPC #1) currents, respectively.

g, h Potential-capacity profiles of IAF Li metal coin cells with high loading SCNMC811 positive electrodes and charged through CC (CC #1) and MPC (MPC #1) currents, respectively. **i, j** Potential-time profiles of NMC622 IAF Li metal coin cells aging at the discharge state, which was charged through CC and MPC currents, respectively. **k, l** Coulombic efficiencies of calendar-aged IAF Li metal coin cells with high loading NMC622 positive electrodes and SCNMC811 positive electrodes, respectively.

and 2 GPa, respectively. The SEI yield strength is defined as 1% of the modulus⁶⁰, and the Von Mises criterion was employed for the determination of SEI failure⁶¹. As shown in Fig. 4a–c, with 0.75 mAh cm⁻² of Li metal deposited at 1 mA cm⁻² continuously, the yield strength of SEI was reached, which means that the SEI at this stage would be pierced and form the dendritic Li. By contrast, the accumulated stress of the 0.5 mA cm⁻² (0.25 mAh cm⁻²) - 1 mA cm⁻² (0.5 mAh cm⁻²) sample (Fig. 4d–f) is far below its yield strength, indicating that the higher modulus of SEI formed at lower current density could change the deposition electrochemical potential and boost Li metal uniformity. The simulation results show that the poor SEI strength formed by large current density (1 mA cm⁻²) cannot sustain the continuous current surge during the Li metal plating process, leading to the formation of porous Li metal deposition and a thick by-product layer on cycled LMNE. However, the strong SEI with high strength which was formed at a small current density (0.5 mA cm⁻²) can sustain the current surge during the continuous Li metal plating process, forming the densified Li metal deposition and thin by-product layer on cycled LMNE.

If we set the first 0.25 mAh cm⁻² of Li deposited at 0.5 mA cm⁻² with various SEI modulus and roughness, the maximum allowable current density (MACD) for the following Li deposition at 0.5 mAh cm⁻² can be screened out (Fig. 4g, Supplementary Figs. 30–31). The results show that the high modulus and small roughness of SEI can increase the MACD. With the SEI modulus of 10 GPa and SEI amplitude (A) of 40 nm, the MACD could be as high as -3.8 mA cm⁻² (Supplementary Fig. 30). The simulated results are consistent with the Li metal morphologies shown in Fig. 4h, i and

Supplementary Fig. 32, where the SEI formed at 0.5 mA cm⁻² could sustain the current surge at 2 mA cm⁻² and 3 mA cm⁻², while the SEI formed at 1 mA cm⁻² could not sustain the current surge even at 0.5 mA cm⁻² and generate the porous Li metal.

Performance of IAF Li metal coin cells

The MPC charging protocol was further applied to cycle IAF Li metal coin cells coupled with two high mass loading layered oxide positive electrodes, such as polycrystalline LiNi_{0.6}Mn_{0.2}Co_{0.2}O₂ (NMC622, 28 mg cm⁻²) and single crystal LiNi_{0.8}Mn_{0.1}Co_{0.1}O₂ (SCNMC811, 26 mg cm⁻²). In addition to the constant charge mechanism at 1 mA cm⁻² (CC, Fig. 5a), one MPC charge protocol was also proposed for IAF Li metal coin cells, as shown in Fig. 5b. The CC and MPC protocols demonstrate a similar tendency as that in the CC and MPC plating protocols for Li||Cu cells, respectively. As expected, the IAF Li metal coin cell charged through the MPC protocol showed a significantly better performance, delivering a longer cycle life and higher CEs (Fig. 5c, d). According to the potential-capacity profiles of the tested IAF Li metal coin cells, batteries charged through CC protocol demonstrate a faster capacity decay than those charged with MPC protocol (Fig. 5e–h). The morphologies of the 2nd plated LMNE in Cu||NMC622 full cell were also characterized by SEM. As shown in Supplementary Fig. 33a–d, the charged LMNE through CC protocol exhibits a porous surface, which is different from the flat surface of the MPC-charged one. After 20 cycles, the cycled negative electrode through CC protocol has more “dead Li” formation and thicker by-product layer than the MPC cycled negative electrode

(Supplementary Fig. 33e–l), leading to the observed inferior cycling performance.

A constant capacity-constant potential charge for both the CC and MPC protocols was also designed to approximate the dynamic 100% SoC charge of Cu|NMC622 full cells, as shown in Supplementary Fig. 34. The cycling results clearly show that the MPC charged cell delivered better capacity retention than the CC charged cell, showing the merits of MPC protocol. The MPC protocol is also effective in decreasing the potential polarizations of LMBs with C@S positive electrode (Supplementary Fig. 35) and NMC622 positive electrode (Supplementary Fig. 36), and extending their cycle life. The cycling stability of graphite negative electrode under fast-charge conditions can also be increased via MPC charge protocol (Supplementary Fig. 37). The existence of lithium inventory at the lithiated and delithiated state of cycled graphite negative electrode was clearly reduced (Supplementary Fig. 38).

Extended applications

The MPC charging protocol is also applicable in the following categories: i) Prevent over-discharge; ii) IAF Li metal pouch cells. Upon calendar aging of 48 hours for the cycled IAF Li metal coin cells, severe over-discharge of the IAF Li metal coin cells charged through CC protocol was found (Fig. 5i, Supplementary Fig. 39c and Supplementary Fig. 40c, e), while such over-discharging is effectively suppressed through MPC charging (Fig. 5j, Supplementary Fig. 39d and Supplementary Fig. 40d, f). Moreover, as shown in Fig. 5k, l, the first cycle CEs of the IAF Li metal coin cells charged through MPC protocol after calendar aging is larger than the former ones (94.2% compared to 95.9% of CC protocol and 101.2% compared to 97.3% of MPC protocol in NMC622 IAF Li metal coin cells, and 94.3% compared to 96.1% of CC protocol and 99.8% compared to 98% of MPC protocol in SCNM811 IAF Li metal coin cells), indicating that dead Li formed in the former cycles has been re-utilized by MPC protocol, while this is not the case for IAF Li metal coin cells charged through CC protocol. It is worth noting that for polycrystalline NMC622 (Supplementary Fig. 39a, b) or single-crystalline NMC811 positive electrode materials (Supplementary Fig. 40a, b), the above capacity-recovery performances of IAFLMBs can be achieved repeatedly. Since this reactivation process was carried out at the discharge state of LMBs, where the safety concerns of battery have been largely decreased compared to the battery with high SoC⁶². Therefore, it is easy to reactivate the dead Li across multiple modules in a large-scale battery without the need for other protection techniques.

A gradient MPC charging protocol (1.5 Ah–1.2 Ah–0.9 Ah) was further developed to charge-discharge 1.8 Ah (370 Wh kg⁻¹) IAF Li metal pouch cells using a commercial-scale NMC622 positive electrodes (Supplementary Table 4). The cells were tested using conventional carbonate electrolyte (1 M LiPF₆ in EC/DEC (v/v, 1/1) with 10 wt% FEC) and under a stack pressure of 800 kPa (Supplementary Fig. 41a, c). The results show that the MPC charge protocol could elongate its cycling life of 32 cycles for CC charge to 66 cycles and possess significantly higher CEs (98.5% compared to 97.5% of CC protocol, Fig. 6a–d). Although the state-of-charge (SoC) for the present CC or MPC charge protocol of IAF Li metal pouch cell is less than 100%, the IAF Li metal coin cell that was charged-discharged at 0.2 C (5 h charge) and 100% SoC (between 2.8 and 4.3 V) can only maintain 55.4% of its capacity after 30 cycles (Supplementary Fig. 42), which further shows the advantage of the MPC protocol in improving the cycling stability of IAFLMBs. In addition, the MPC charge protocol can improve the capacity retention of IAF Li metal pouch cell under ambient pressure conditions (Supplementary Fig. 41b, d), which could be cycled longer, especially at the high-capacity regime (Supplementary Fig. 43c–f). Replacing the conventional electrolyte with high concentration dual-salt electrolyte (2 M LiDFOB and 1.4 M LiBF₄ in FEC/DEC (v/v, 1/2))²³, the 1.5 Ah (400 Wh kg⁻¹) IAF Li metal pouch

cell with SoC of 80% could retain 80% of its capacity even after 298 cycles, which represents a significant advance over the reported IAF Li metal pouch cells^{10,23–26,63–69} (Fig. 6e, f and Supplementary Tables 4, 5).

Although the high current density at the middle step of charging process would produce more heat during the charge process, the temperature increase (-0.5 °C) is bearable for the charging station (Supplementary Fig. 44b). Whereas its smaller discharge temperature variation (-27.5 °C for MPC protocol versus -29 °C for CC protocol) would benefit the service of battery during the discharge process. The pouch cell charged by MPC protocol delivered smaller potential polarizations when varying the pressure conditions (33 and 46.1 mV compared to 49 and 74.6 mV of CC protocol, respectively, Fig. 6a, b and Supplementary Fig. 43a, b). The smaller volume expansions for the cell charged through MPC protocol (Supplementary Fig. 45) is attributed to the thinner reaction by-product layer on the extracted separator for the terminated pouch cell (Supplementary Fig. 46), demonstrating the merit of the MPC protocol in suppressing the side-reactions during the cycling process. The failure mechanism of IAFLMBs and LMBs that were charged via CC current was different. As shown in Supplementary Fig. 47a, b, for both cycling protocols of CC and MPC, the IAFLMBs can still be operated continuously even though the terminated charge potential has reached 5 V vs. Li⁺/Li. This clearly shows that the IAFLMBs will fail gradually during the continuous cycling process. However, for the LMBs with N/P ratio of -0.5 (Supplementary Fig. 47c, d), the cell with CC protocol displays an abrupt failure after its terminated charge potential reaching 5 V vs. Li⁺/Li, while the LMB cell with MPC protocol exhibits a gradual failure mechanism. The reason for the difference in failure modes between CC charged IAFLMBs and LMBs should originate from the difference in Li metal capacity. Due to the low capacity of active Li metal, the LMNE in IAFLMBs will corrode quickly, resulting in a shorter cycling life compared to LMBs. The short cycle life of IAFLMBs lies in its thinner by-product layer, which may be incapable of piercing through polymer separator and incur battery short-circuit. For LMBs, although its life will be longer, the accumulated by-product layer on the surface of LMNE will be more serious than that in IAFLMBs, which may incur the short-circuit of LMBs and result in the abrupt failure of LMBs eventually. The present MPC protocol exhibits high potential of practical applications in terms of the charge time, maximum charge power and cycling performance (Supplementary Figs. 3, 4 and Supplementary Tables 6, 7). The present research does provide extensive evidence to prove the effectiveness of MPC for enhancing the cycling stability of IAF LMBs, which could enlighten a bright future for its practical applications.

The formation of porous Li metal negative electrode (LMNE) was captured to happen upon continuous conventional CC charge of LMNE, leading to a porous Li metal structure with a large surface area. Upon further cycling, LMBs charged through CC protocol suffer from low CE, thick by-products and short life eventually. Whereas, for the MPC protocol of LMBs, the SEI formed at the initial stage possesses high strength and is capable of protecting it from current surging, directing the densified Li deposition with a small surface area and dense packing. When an IAF Li metal coin cell is charged via the MPC protocol, it delivers high CEs, thin by-products and long cycle life. In addition, this protocol is applicable for preventing over-discharge and gradient charging of a large Li metal pouch cell with initially anode-free configuration (1.5 Ah (400 Wh kg⁻¹)). This strategy provides both methodological and conceptual advancements for the development of high-performance LMBs, example of which could have a broad impact on not only liquid batteries, but also facilities such as safe high-energy solid-state batteries, portable devices and chemical or electrochemical reactions with limiting factors such as time, space and materials transfer.

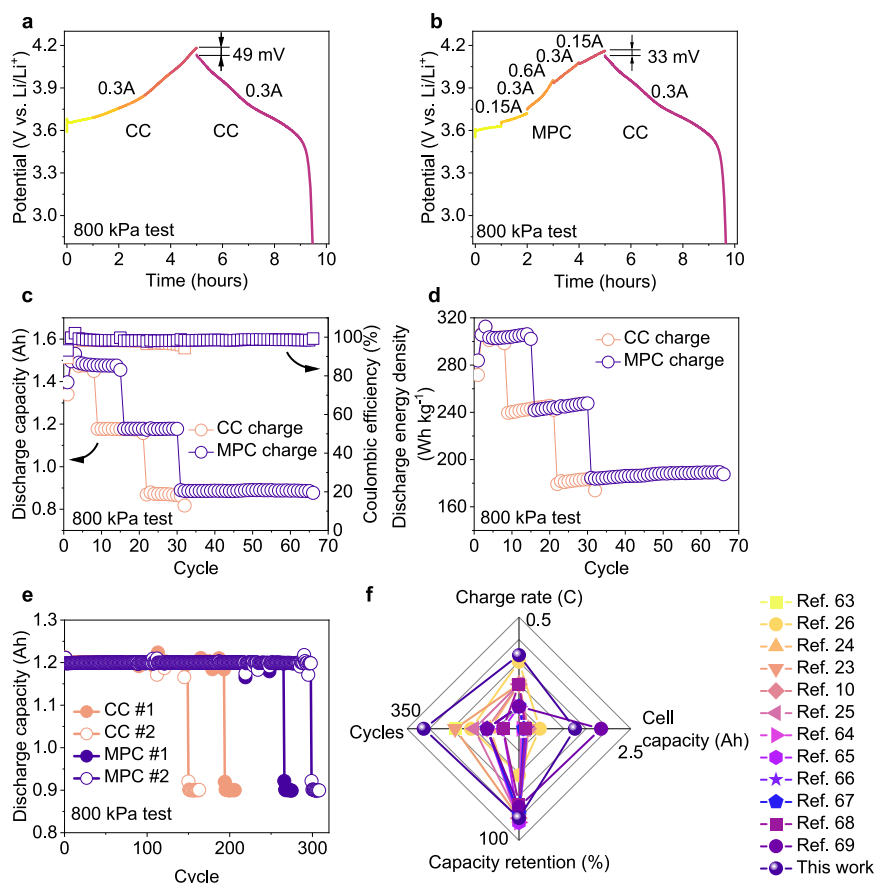


Fig. 6 | Cycling performance of IAF Li metal pouch cells. **a, b** The 1st cycle charge-discharge potential-time profiles of 1.8 Ah IAF Li metal pouch cells with NMC622 positive electrode tested at high-pressure conditions, which was charged through CC and MPC protocol, respectively, and then discharged with CC protocol at 0.3 A. **c, d** Discharge capacity and coulombic efficiency, and Discharge energy density of 1.8 Ah IAF Li metal pouch cell tested under high-pressure conditions with different

charge protocols and the same discharge protocol (Supplementary Table 4), the electrolyte here is 1 M LiPF_6 in EC/DEC (v/v, 1/1) with 10 wt% FEC. **e** Discharge capacity and Coulombic efficiency of 1.5 Ah IAF Li metal pouch cell tested under high-pressure conditions, the electrolyte here is 2 M LiDFOB and 1.4 M LiBF_4 in FEC/DEC (v/v, 1/2). **f** Comparison for the cycling performance of current work with existing results.

Methods

Materials

Dehydrated alcohol solvent, N-methylpyrrolidone (NMP) solvent, fluoroethylene carbonate (FEC) and LiNO_3 particles with analytical grade were purchased from Aladdin (Shanghai, China). The copper foil (thickness: $\sim 10 \mu\text{m}$), aluminum foil (thickness: $\sim 20 \mu\text{m}$), carbon black (Super P), carbon nanotubes (CNTs), polypropylene (PP, Celgard 2400) separator (thickness: $\sim 20 \mu\text{m}$), double ceramic (Al_2O_3)-coated PP membrane (with film thickness of $14 \mu\text{m}$ and coating thickness of $3 \mu\text{m}$), polycrystalline $\text{LiNi}_{0.6}\text{Mn}_{0.2}\text{Co}_{0.2}\text{O}_2$ powder, single-crystalline $\text{LiNi}_{0.8}\text{Mn}_{0.1}\text{Co}_{0.1}\text{O}_2$ powder, 2032-type coin-cell cases, springs, and spacers and metallic foil (with diameter of 16 mm and thickness of $100 \mu\text{m}$, Li content $\geq 99.9\%$) were purchased from Canrd Technology Co. Ltd. The electrolyte of 1 M lithium bis(trifluoromethanesulfonyl) imide (LiTFSI) in DOL/DME = 1/1 vol, 1 M lithium hexafluorophosphate (LiPF_6) in EC/DEC (v/v, 1/1), and polyvinylidene difluoride (PVDF 5130, MW = 1,300,000) were purchased from DodoChem. All solvents were stored over 4 Å molecular sieves for 48 h before use. All the electrolytes were prepared in a glove box filled with argon gas ($\text{H}_2\text{O} < 0.1 \text{ ppm}$, $\text{O}_2 < 0.1 \text{ ppm}$).

Preparation of negative electrodes, positive electrodes, and separators

To prepare Cu current collectors, commercial Cu foil was punched into slices 12 mm and 16 mm in diameter, respectively. Then the obtained Cu slices were immersed in anhydrous alcohol. After 30 min of

ultrasonic washing, they were dried in a vacuum oven at 60°C for 12 h. Afterwards, the Cu slices were transferred to a glovebox ($\text{H}_2\text{O} < 0.1 \text{ ppm}$, $\text{O}_2 < 0.1 \text{ ppm}$) for future usage.

The high loading $\text{LiNi}_{0.6}\text{Mn}_{0.2}\text{Co}_{0.2}\text{O}_2$ (NMC622, 28 mg cm^{-2}) and single crystal $\text{LiNi}_{0.8}\text{Mn}_{0.1}\text{Co}_{0.1}\text{O}_2$ (SCNMC811, 26 mg cm^{-2}) positive electrodes were prepared via the slurry-coating method. Typically, the pre-dried active material (NMC622 and SCNMC811), Super P and PVDF were mixed in a mass ratio of 8:1:1. After grinding in a mortar, stir mixing with NMP in a beaker for 6 h, the as-formed slurries were blade-coated on the Al foil. Upon evaporation of NMP in an oven at 80°C , the Al supported positive electrodes were punched into slices 12 mm in diameter. Upon weighing and further drying in vacuum oven at 60°C for 12 h, these slices were transferred to the glovebox. Before usage, the PP was punched into slices with diameter of 19 mm. After being washed with anhydrous alcohol and further dried in the vacuum oven at 60°C for 12 h, it was transferred to the glovebox for future usage.

Assembly of coin cells

To evaluate the CEs, Cu foil (12 mm) was matched with Li foil to assemble CR2032 coin cells. The separator used here is PP, and the electrolyte for Li||Cu cells is 1 M LiTFSI in DOL/DME (v/v, 1/1) with 1 wt% LiNO_3 , if not stated otherwise. Initially anode-free (IAF) Li metal coin cells were fabricated by matching high loading positive electrodes (NMC622 or SCNMC811) with Cu foil (16 mm) directly. The electrolyte employed here is 1 M LiPF_6 in EC/DEC (v/v, 1/1) with 10 wt% FEC. In this research, 60 μL s of electrolyte were used for coin cell tests. To evaluate

the cycling performances of Li metal cells (with N/P ration of 0.6), the Cu@Li anodes were prepared first. Typically, two Li||Cu half cells with the electrolyte of 1 M LiPF₆ in EC/DEC (v/v, 1/1) with 10 wt% FEC were assembled. After five cycles of activation at 0.05 mA cm⁻² within the potential range of 0.01–1 V vs. Li⁺/Li, Li metal was plated on the Cu foil at 3 mAh cm⁻² via CC current in both Li||Cu half cells. Then, the as-formed Cu@Li negative electrodes can be obtained by disassembling these two half cells.

Assembly of IAF Li metal pouch cells

The preparation of 1.8 Ah (370 Wh kg⁻¹, -18 g in total mass) IAF Li metal pouch cells was carried out in Guangdong Graphene Innovation Center. Typically, the dried NMC622 particles were mixed with PVDF, Super P and carbon nanotubes (CNTs) at a mass ratio of 95:3:1.8:0.2, respectively. After mixing with NMP to form a homogenous slurry, it was coated on the Al foil (16 μm) double-sided with an areal-loading of 30 mg cm⁻². After drying, the coatings were sliced into NMC622 positive electrode (56 mm × 657 mm). The thickness of the Cu foil used in the present IAF Li metal pouch cell is 9 μm, with dimensions of 58 mm × 570 mm. Then the above electrodes were wound with a ceramic-coated PP membrane. The width of the rolling needle is 34 mm and the amount of rolling layer is 14. Upon assembled with Al-plastic film and injected with electrolyte (1 M LiPF₆ in EC/DEC (1/1, v/v) with 10 wt% FEC, 3 g Ah⁻¹), the un-activated IAF Li metal pouch cells were obtained. Before ex-factory test, these cells were first charged to 4.3 V at a current of 225 mA and then discharged to 3.0 V at the same current, as shown in Supplementary Fig. 43a.

For the preparation of 1.5 Ah (400 Wh kg⁻¹, -12 g in total mass) IAF Li metal pouch cells, the dried LiNi_{0.9}Mn_{0.05}Co_{0.05}O₂ (NMC90) particles (provided by Guangdong Graphene Innovation Center) were mixed with PVDF, Super P and carbon nanotubes (CNTs) at mass ratio of 95:3:1.8:0.2, respectively. After mixing with NMP to form a homogeneous slurry, it was coated on the Al foil (10 μm) double-sided with areal loading of 22 mg cm⁻². After drying, the coatings were sliced into NMC90 positive electrode (56 × 567 mm). The bare Cu foil (9 μm) was sliced into a negative electrode with dimensions of 59 × 475 mm. Then the above electrodes were wound with PP membrane. The number of rolling layers is 12. Upon assembled with Al-plastic film and injection with electrolyte (2 M LiDFOB and 1.4 M LiBF₄ in FEC/DEC (v/v, 1/2)²³, 2 g Ah⁻¹), the un-activated IAF Li metal pouch cells were obtained. Before the ex-factory test, these cells were first charged to 4.5 V at a current of 225 mA and then discharged to 3.0 V at the same current, as shown in Supplementary Fig. 43b.

Characterization

X-ray photoelectron spectroscopy (XPS) was adopted to explore the chemical information of SEI and cycled electrodes. A PHI5000 VersaProbe II XPS with Al Kα irradiation (1486.6 eV) was employed. SEM was utilized to characterize the morphologies of Li metal and the cycled electrode morphologies by using a cold field scanning electron microscope (SU8010, HITACHI) at 5 kV. AFM characterization was carried out to determine the surface fluctuation and Young's modulus of SEI. Typically, the facility (Bruker, DIMENSION ICON) was placed in an Ar-filled glovebox (MBRAUN, H₂O < 0.1 ppm, O₂ < 0.1 ppm), and the AFM images were collected based on the PeakForce tapping mode. The modulus was obtained through the quantitative nanomechanics mode (QNM) and further fitting the curve using Derjaguin-Muller-Toropov (DMT) model. As an extension of the PeakForce tapping mode, the QNM can provide the modulus maps by analyzing the force at each scan point. It is worth noting that the preparation and ex-situ measurements of the electrode samples were carried out at a temperature range of 25 ± 1 °C. As to the electrochemical impedance spectrum (EIS) test, the Li||Cu cells were fabricated and cycled 5 times at 0.05 mA cm⁻² within the potential of 0.01 V and 1 V firstly. Then, a fixed capacity of Li metal (0.25 mAh cm⁻²

or 3 mAh cm⁻²) was deposited on Cu foil through CC or MPC protocol, respectively. The Li||Cu@Li cells were kept under -20 °C, -10 °C, 0 °C, 10 °C, 20 °C, 30 °C to record the temperature-dependent EISs (with a frequency range from 100,000 Hz to 0.1 Hz and an amplitude of 5 mV (potentiostatic, Steps/Decade = 10, quasi-stationary potential)).

Electrochemical tests

All the Li||Cu half cells were cycled five times at 0.05 mA cm⁻² within the potential between 0.01 V and 1 V before further test. For the Coulombic efficiency (CE) test, Li metal was deposited on Cu foil at 3 mAh cm⁻² through each protocol and followed with stripping to 1 V at 1 mA cm⁻². The plating current densities are listed in Supplementary Table 1. To test the average CEs, the Li||Cu cells were pre-cycled one time through CC-1mA (6 h) and MPC-2mA-3rd (6 h): 0.5 mA cm⁻² (1 h)-1 mA cm⁻² (1 h)-2 mA cm⁻² (1 h)-1.5 mA cm⁻² (1 h)-0.5 mA cm⁻² (1 h)-0.5 mA cm⁻² (1 h) protocols (both charged to 1 V at 1 mA cm⁻²), respectively. Then Li (Q_T) was deposited on Cu foil at 6 mAh cm⁻² through CC-1mA (6 h) and MPC-2mA-3rd (6 h), followed by charge-discharge with a capacity of 3 mAh cm⁻² (Q_C) for 11 cycles through CC (3 h) or MPC (3 h) protocols. Finally, the capacity when stripping to 1 V was measured (capacity: Q_S), and the average CEs can be calculated as: (11Q_C + Q_S) / (11Q_C + Q_T).

To compare the electrochemical performance of different charge protocols such as the pulsed current^{36,70}, the asymmetrical bidirectional current³⁸, the self-heat current⁴⁰-9 mA cm⁻², the seed current⁴¹-20 mA cm⁻², the seed current⁴²-50 mA cm⁻² and the middle peak current in present research, Cu foil (12 mm) was matched with Li foil to assemble Li||Cu coin cells. Typically, the electrolyte here is 1 M LiPF₆ in EC/DEC (1/1, v/v) with 10 wt% FEC, which is the same as the electrolyte for IAF Li metal coin cells. The test methods for these protocols are listed as follows: CC current, with continuous constant plating current of 1 mA cm⁻²; Asymmetric bidirectional charge protocol, with Li metal deposited at 1 mA cm⁻² for 0.5 h and then it was followed by stripping Li metal at 1 mA cm⁻² for 2 min (120 s), which was repeated 6 times and then followed by plating Li metal at 1 mA cm⁻² for 12 min (720 s); Pulsed charge protocol, with Li metal deposited at 1 mA cm⁻² for 0.5 h and then it was followed by remaining open circuit potential (OCP) for 2 min, which was repeated 6 times; Self heat-9 mA cm⁻² charge protocol, with Li metal deposited at 9 mA cm⁻²; Seed current-20 mA cm⁻² charge protocol (20 mA-1 mA), with Li metal deposited at 20 mA cm⁻² for 3 min (180 s) firstly and then it was followed by plating Li metal at 1 mA cm⁻²; Seed current-50 mA cm⁻² charge protocol (50 mA-1 mA), with Li metal deposited at 50 mA cm⁻² for 4 s firstly and then it was followed by plating Li metal at 1 mA cm⁻²; MPC charge protocol, with Li metal deposited at 0.5 mA cm⁻² for 0.5 h, 1 mA cm⁻² for 0.5 h, 2 mA cm⁻² for 0.5 h, 1.5 mA cm⁻² for 0.5 h and 0.5 mA cm⁻² for 1 h continuously. It is worth noting that for all these plating protocols, the total amount of Li metal deposited is 3 mAh cm⁻² and the deposited Li metal was stripped at 1 mA cm⁻² until the potential of Li||Cu half cells reach 1 V.

For the charge-discharge of IAF Li metal coin cells and Li metal coin cells, all the cells were charged for 3 hours with specified charge protocol and then discharged to 2.8 V (NMC622, SCNMC811) at 1 mA cm⁻². For the 0.2 C charge-discharge of IAF Li metal coin cells (with NMC622 positive electrode) between 2.8 and 4.3 V (100 SoC) and under CC, the charge-discharge current was based on the theoretical capacity of 180 mAh g⁻¹ for NMC622. For the 1.8 Ah IAF Li metal pouch cells, 5 hours gradient charge with Li capacity of 1.5 Ah, 1.2 Ah and 0.9 Ah were carried out sequentially. In addition, for the 1.5 Ah IAF Li metal pouch cells, 3 hours gradient charge with Li capacity of 1.2 Ah and 0.9 Ah were carried out sequentially. Details for pouch cell test are available in Supplementary Table 4. All the coin and pouch cells were cycled at the temperature range of 25 ± 1 °C.

Simulation

The simulation domain of electrolyte/separator is shown in Supplementary Fig. 14. The non-uniform SEI surface is mimicked by a cosine function with amplitude A ($y = 200 + A \cos \omega \pi x$, where $\omega = 1.3$ and $A = 40$ or 50 nm). The current density boundary condition and symmetric boundary are applied to the top boundary and the two side-boundaries, respectively.

The ternary current distribution, deformed geometry and solid mechanics modules of COMSOL multiphysics were used in simulation of the plating/stripping of Li and the mechanical response of SEI. Charge and species conservation laws govern the evolution of concentration and electrical potential with ion flux given by Nernst-Planck equation⁷¹:

$$J_i = -D_i \nabla c_i - z_i u_i F c_i \nabla \phi$$

where subscript i denotes ionic species i , J_i , D_i , c_i , z_i , u_i are the ion flux, diffusion coefficient, concentration, charge carried, and mobility of species ionic species i , respectively. F is the Faraday's constant and ϕ is the electrical potential of electrolyte.

Butler-Volmer equation was utilized to describe the electrochemical kinetics at interface:

$$i_{\text{loc}} = i_0 \left(C_R \exp\left(\frac{\alpha_a F \eta}{RT}\right) - C_O \exp\left(\frac{-\alpha_c F \eta}{RT}\right) \right)$$

where i_{loc} is the local current density; i_0 is the exchange current density; η is the reaction overpotential; α_a and α_c are the transfer coefficients for anodic and cathodic reactions, respectively; C_R and C_O are the dimensionless concentration, respectively; R is the idea gas constant; and T is the absolute temperature.

The SEI was considered as an elastic material⁶⁰. The thickness of Li deposition is calculated by the ternary current distribution and deformed geometry modules of COMSOL and is imposed as the prescribed normal displacement at the SEI-Li interface. No initial residual stress is considered in SEI. Stress distribution in the domain was solved by quasi-static assumption:

$$\nabla \cdot \sigma = 0$$

where σ is the Cauchy stress tensor.

The influence of deformed SEI on electrochemical kinetics is taken into account by introducing a factor term in the Butler-Volmer equation^{72,73}:

$$B = \exp\left(\frac{\gamma \Delta \mu_e}{RT}\right)$$

where the electrochemical potential change $\Delta \mu_e$ resulting from local strain is assumed to be proportional to the Young's modulus of SEI. A form of $B = \exp\left(\kappa \frac{E_{\text{SEI}} - E_0}{E_0}\right)$ is adopted for illustrative purpose. If modulus of SEI is higher than the modulus E_0 , its effect on electrochemical potential change is included. Value of E_0 is taken as 1 GPa and scaling parameter κ takes the value of -0.3. Other parameters used in the simulation are listed in Supplementary Table 3.

To obtain the maximum allowable current density (MACD) for the SEI with various modulus and SEI roughness, the first 0.25 mAh cm⁻² of Li was deposited at 0.5 mA cm⁻², then the following 0.5 mAh cm⁻² of Li was further deposited at various current densities. The Von Mises criterion was employed for the determination of SEI failure⁶¹. Through continuous simulations at specific SEI modulus and amplitude, one could get the MACD for the following 0.5 mAh cm⁻² of Li metal plating.

Data availability

The authors declare that the main data supporting our findings of this study are contained within the paper and Supplementary Information. The source data generated in this study are provided in the Source Data file. Source data are provided with this paper.

References

- Whittingham, M. S. Electrical energy storage and intercalation chemistry. *Science* **192**, 1126 (1976).
- Mizushima, K. et al. Li_xCoO₂ (0 < x ≤ 1): a new cathode material for batteries of high energy density. *Mater. Res. Bull.* **15**, 783–789 (1980).
- Bruce, P. G. et al. Li-O₂ and Li-S batteries with high energy storage. *Nat. Mater.* **11**, 19–29 (2011).
- Jäckle, M. et al. Self-diffusion barriers: possible descriptors for dendrite growth in batteries? *Energy Environ. Sci.* **11**, 3400–3407 (2018).
- Wu, H. et al. Recent progress in understanding solid electrolyte interphase on lithium metal anodes. *Adv. Energy Mater.* **11**, 2003092 (2021).
- Yoon, G. et al. Deposition and stripping behavior of lithium metal in electrochemical system: continuum mechanics study. *Chem. Mater.* **30**, 6769–6776 (2018).
- Wang, X. et al. Glassy Li metal anode for high-performance rechargeable Li batteries. *Nat. Mater.* **19**, 1339–1345 (2020).
- Xue, W. et al. Ultra-high-voltage Ni-rich layered cathodes in practical Li metal batteries enabled by a sulfonamide-based electrolyte. *Nat. Energy* **6**, 495–505 (2021).
- Rustomji, C. et al. Liquefied gas electrolytes for electrochemical energy storage devices. *Science* **356**, eaal4263 (2017).
- Yu, Z. et al. Molecular design for electrolyte solvents enabling energy-dense and long-cycling lithium metal batteries. *Nat. Energy* **5**, 526–533 (2020).
- Chen, S. et al. High-voltage lithium-metal batteries enabled by localized high-concentration electrolytes. *Adv. Mater.* **30**, 1706102 (2018).
- Kim, M. S. et al. Langmuir–Blodgett artificial solid-electrolyte interphases for practical lithium metal batteries. *Nat. Energy* **3**, 889–898 (2018).
- Gao, Y. et al. Low-temperature and high-rate-charging lithium metal batteries enabled by an electrochemically active monolayer-regulated interface. *Nat. Energy* **5**, 534–542 (2020).
- Yang, C. et al. Ultrafine silver nanoparticles for seeded lithium deposition toward stable lithium metal anode. *Adv. Mater.* **29**, 1702714 (2017).
- Yan, K. et al. Selective deposition and stable encapsulation of lithium through heterogeneous seeded growth. *Nat. Energy* **1**, 16010 (2016).
- Liu, Y. et al. In-plane highly dispersed Cu₂O nanoparticles for seeded lithium deposition. *Nano Lett.* **19**, 4601–4607 (2019).
- Zhang, R. et al. Lithiophilic sites in doped graphene guide uniform lithium nucleation for dendrite-free lithium metal anodes. *Angew. Chem. Int. Ed. Engl.* **56**, 7764–7768 (2017).
- Liu, Y. et al. Oxygen and nitrogen co-doped porous carbon granules enabling dendrite-free lithium metal anode. *Energy Storage Mater.* **18**, 320–327 (2019).
- Kozen, A. C. et al. Next-generation lithium metal anode engineering via atomic layer deposition. *ACS Nano* **9**, 5884–5892 (2015).
- Qian, J. et al. Anode-free rechargeable lithium metal batteries. *Adv. Funct. Mater.* **26**, 7094–7102 (2016).
- Louli, A. J. et al. Exploring the impact of mechanical pressure on the performance of anode-free lithium metal cells. *J. Electrochem. Soc.* **166**, A1291–A1299 (2019).

22. Zhao, C. et al. A high-energy and long-cycling lithium–sulfur pouch cell via a macroporous catalytic cathode with double-end binding sites. *Nat. Nanotechnol.* **16**, 166–173 (2021).
23. Louli, A. J. et al. Diagnosing and correcting anode-free cell failure via electrolyte and morphological analysis. *Nat. Energy* **5**, 693–702 (2020).
24. Weber, R. et al. Long cycle life and dendrite-free lithium morphology in anode-free lithium pouch cells enabled by a dual-salt liquid electrolyte. *Nat. Energy* **4**, 683–689 (2019).
25. Yu, Z. et al. Rational solvent molecule tuning for high-performance lithium metal battery electrolytes. *Nat. Energy* **7**, 94–106 (2022).
26. Xu, R. et al. Designing and demystifying the lithium metal interface toward highly reversible batteries. *Adv. Mater.* **33**, 2105962 (2021).
27. Guo, Z. et al. Optimal charging method for lithium ion batteries using a universal voltage protocol accommodating aging. *J. Power Sources* **274**, 957–964 (2015).
28. Yin, Y. et al. New fast charging method of lithium-ion batteries based on a reduced order electrochemical model considering side reaction. *J. Power Sources* **423**, 367–379 (2019).
29. Wang, S. et al. A model-based continuous differentiable current charging approach for electric vehicles in direct current microgrids. *J. Power Sources* **482**, 229019 (2021).
30. Aurbach, D. et al. Factors which limit the cycle life of rechargeable lithium (metal) batteries. *J. Electrochem. Soc.* **147**, 1274 (2000).
31. Lu, D. et al. Failure mechanism for fast-charged lithium metal batteries with liquid electrolytes. *Adv. Energy Mater.* **5**, 1400993 (2015).
32. Shi, F. et al. Lithium metal stripping beneath the solid electrolyte interphase. *Proc. Natl. Acad. Sci.* **115**, 8529 (2018).
33. Louli, A. J. et al. Optimizing cycling conditions for anode-free lithium metal cells. *J. Electrochem. Soc.* **168**, 020515 (2021).
34. Liu, F. et al. Dynamic spatial progression of isolated lithium during battery operations. *Nature* **600**, 659–663 (2021).
35. Zhang, W. et al. Recovery of isolated lithium through discharged state calendar ageing. *Nature* **626**, 306–312 (2024).
36. Mayers, M. Z. et al. Suppression of dendrite formation via pulse charging in rechargeable lithium metal batteries. *J. Phys. Chem. C.* **116**, 26214–26221 (2012).
37. GarcC-a, G. et al. Exceeding 6500 cycles for LiFePO₄/Li metal batteries through understanding pulsed charging protocols. *J. Mater. Chem. A* **6**, 4746–4751 (2018).
38. Wang, D. et al. Synchronous healing of Li metal anode via asymmetrical bidirectional current. *iScience*, **23**, 100781 (2019).
39. Park, S. H. & Lee, Y. J. Morphological control of electrodeposited lithium metal via seeded growth: stepwise spherical to fibrous lithium growth. *J. Mater. Chem. A* **9**, 1803–1811 (2021).
40. Li, L. et al. Self-heating–induced healing of lithium dendrites. *Science* **359**, 1513–1516 (2018).
41. Huang, Z. et al. Seeding lithium seeds towards uniform lithium deposition for stable lithium metal anodes. *Nano Energy* **61**, 47–53 (2019).
42. Yuan, X. et al. Ultrafast deposition of faceted lithium polyhedra by outpacing SEI formation. *Nature* **620**, 86–91 (2023).
43. Stein, H. S. C. r. Nonlinear potentiodynamic battery charging protocols for fun, education, and application. *ACS Eng. Au* **4**, 345–350 (2024).
44. Shin, J. W. & Chason, E. Compressive stress generation in Sn thin films and the role of grain boundary diffusion. *Phys. Rev. Lett.* **103**, 056102 (2009).
45. Chason, E. et al. Understanding residual stress in electrodeposited Cu thin films. *J. Electrochem. Soc.* **160**, D3285 (2013).
46. Janssen, G. C. A. M. Stress and strain in polycrystalline thin films. *Thin Solid Films* **515**, 6654–6664 (2007).
47. Spaepen, F. Interfaces and stresses in thin films. *Acta Mater.* **48**, 31–42 (2000).
48. Abadias, G. et al. Review article: stress in thin films and coatings: current status, challenges, and prospects. *J. Vac. Sci. Tec., hnoI. A* **36**, 020801 (2018).
49. Wang, X. et al. Stress-driven lithium dendrite growth mechanism and dendrite mitigation by electroplating on soft substrates. *Nat. Energy* **3**, 227–235 (2018).
50. Hebert, K. R. Diffusion and creep in lithium metal anodes induced by plating and stripping reactions. *J. Electrochem. Soc.* **170**, 110537 (2023).
51. Liu, Y. et al. Horizontal stress release for protuberance-free Li metal anode. *Adv. Funct. Mater.* **30**, 2002522 (2020).
52. Wang, S. et al. Nanoscale observation of the solid electrolyte interface and lithium dendrite nucleation–growth process during the initial lithium electrodeposition. *J. Mater. Chem. A* **8**, 18348–18357 (2020).
53. Dong, K. et al. Unravelling the mechanism of lithium nucleation and growth and the interaction with the solid electrolyte interface. *ACS Energy Lett.* **6**, 1719–1728 (2021).
54. Thornton, J. A. High rate thick film growth. *Annu. Rev. Mater. Sci.* **7**, 239–260 (1977).
55. Yan, C. et al. Regulating the inner helmholtz plane for stable solid electrolyte interphase on lithium metal anodes. *J. Am. Chem. Soc.* **141**, 9422–9429 (2019).
56. Biswal, P. et al. Nucleation and early stage growth of Li electro-deposits. *Nano Lett.* **19**, 8191–8200 (2019).
57. He, M. et al. The intrinsic behavior of lithium fluoride in solid electrolyte interphases on lithium. *Proc. Natl. Acad. Sci. USA* **117**, 73 (2020).
58. Yang, C.-T. & Qi, Y. Maintaining a fat Li surface during the Li stripping process via interface design. *Chem. Mater.* **33**, 2814–2823 (2021).
59. Golozar, M. et al. In situ scanning electron microscopy detection of carbide nature of dendrites in Li–polymer batteries. *Nano Lett.* **18**, 7583–7589 (2018).
60. Shen, X. et al. The failure of solid electrolyte interphase on Li metal anode: structural uniformity or mechanical strength? *Adv. Energy Mater.* **10**, 1903645 (2020).
61. Zhang, Z. F. & Eckert, J. Unified tensile fracture criterion. *Phys. Rev. Lett.* **94**, 094301 (2005).
62. Joshi, T. et al. Safety of lithium-ion cells and batteries at different states-of-charge. *J. Electrochem. Soc.* **167**, 140547 (2020).
63. Genovese, M. et al. Hot formation for improved low temperature cycling of anode-free lithium metal batteries. *J. Electrochem. Soc.* **166**, A3342 (2019).
64. Lin, L. et al. Li-rich Li₂[Ni_{0.8}Co_{0.1}Mn_{0.1}]O₂ for anode-free lithium metal batteries. *Angew. Chem. Int. Ed.* **60**, 8289–8296 (2021).
65. Lin, L. et al. Epitaxial induced plating current-collector lasting lifespan of anode-free lithium metal battery. *Adv. Energy Mater.* **11**, 2003709 (2021).
66. Mao, M. et al. Anion-enrichment interface enables high-voltage anode-free lithium metal batteries. *Nat. Commun.* **14**, 1082 (2023).
67. Mao, M. et al. Electrolyte design combining fluoro- with cyano-substitution solvents for anode-free Li metal batteries. *Proc. Natl. Acad. Sci.* **121**, e2316212121 (2024).
68. Shi, J. et al. In situ p-block protective layer plating in carbonate-based electrolytes enables stable cell cycling in anode-free lithium batteries. *Nat. Mater.* **23**, 1686–1694 (2024).
69. Yang, H. et al. Mitigating overcharge in ampere-hour-level anode-free pouch cells by improving pressure uniformity. *ACS Energy Lett.* **9**, 4331–4338 (2024).
70. Rehnlund, D. et al. Dendrite-free lithium electrode cycling via controlled nucleation in low LiPF₆ concentration electrolytes. *Mater. Today* **21**, 1010–1018 (2018).
71. Newman, J.S. *Electrochemical systems*, Edn. 3rd ed. (Wiley, 2004).

72. Liu, Y. et al. Electro-chemo-mechanical modeling of artificial solid electrolyte interphase to enable uniform electrodeposition of lithium metal anodes. *Adv. Energy Mater.* **12**, 2103589 (2022).
73. Monroe, C. & Newman, J. The impact of elastic deformation on deposition kinetics at lithium/polymer interfaces. *J. Electrochem. Soc.* **152**, A396 (2005).

Acknowledgements

B.H. Li would like to acknowledge the support from National Natural Science Foundation of China (No. 52261160384, 51872157 and 52072208). G.H. Chen acknowledges the financial support from Shenzhen STIC (Grant No. 20190816124333659), Guangdong-HK-Macao Joint (Grant No. 2019B121205001) and National Natural Science Foundation of China and Research Grants Council of Hong Kong joint research program (CityU549/22).

Author contributions

Y.M.L., B.H.L., and G.H.C. conceived and designed this project. B.H.L. and G.H.C. directed the project. Y.M.L. performed the electrode preparation, conducted the material characterizations, carried out the electrochemical measurements and battery tests, wrote the first draft and implemented the revisions. X.G.Y. carried out the COMSOL simulations. S.W.W. conducted the AFM characterizations. All authors participated the writing and revision of manuscript.

Competing interests

The authors declare no competing interests.

Additional information

Supplementary information The online version contains supplementary material available at <https://doi.org/10.1038/s41467-025-66271-0>.

Correspondence and requests for materials should be addressed to Baohua Li or Guohua Chen.

Peer review information *Nature Communications* thanks Jun Xu, Wesley Chang and the other, anonymous, reviewer(s) for their contribution to the peer review of this work. A peer review file is available.

Reprints and permissions information is available at <http://www.nature.com/reprints>

Publisher's note Springer Nature remains neutral with regard to jurisdictional claims in published maps and institutional affiliations.

Open Access This article is licensed under a Creative Commons Attribution-NonCommercial-NoDerivatives 4.0 International License, which permits any non-commercial use, sharing, distribution and reproduction in any medium or format, as long as you give appropriate credit to the original author(s) and the source, provide a link to the Creative Commons licence, and indicate if you modified the licensed material. You do not have permission under this licence to share adapted material derived from this article or parts of it. The images or other third party material in this article are included in the article's Creative Commons licence, unless indicated otherwise in a credit line to the material. If material is not included in the article's Creative Commons licence and your intended use is not permitted by statutory regulation or exceeds the permitted use, you will need to obtain permission directly from the copyright holder. To view a copy of this licence, visit <http://creativecommons.org/licenses/by-nc-nd/4.0/>.

© The Author(s) 2025